

# *Coherence of coronal mass ejections in near-earth space*

Article

Published Version

Creative Commons: Attribution 4.0 (CC-BY)

Open access

Owens, M. J. ORCID: <https://orcid.org/0000-0003-2061-2453>  
(2020) Coherence of coronal mass ejections in near-earth space. Solar Physics, 295. 148. ISSN 0038-0938 doi: 10.1007/s11207-020-01721-0 Available at <https://centaur.reading.ac.uk/93765/>

It is advisable to refer to the publisher's version if you intend to cite from the work. See [Guidance on citing](#).

To link to this article DOI: <http://dx.doi.org/10.1007/s11207-020-01721-0>

Publisher: Springer

All outputs in CentAUR are protected by Intellectual Property Rights law, including copyright law. Copyright and IPR is retained by the creators or other copyright holders. Terms and conditions for use of this material are defined in the [End User Agreement](#).

[www.reading.ac.uk/centaur](http://www.reading.ac.uk/centaur)

**CentAUR**

Central Archive at the University of Reading

Reading's research outputs online



# Coherence of Coronal Mass Ejections in Near-Earth Space

Mathew J. Owens<sup>1</sup> 

Received: 20 July 2020 / Accepted: 16 October 2020 / Published online: 30 October 2020  
© The Author(s) 2020

**Abstract** Interplanetary coronal mass ejections (ICMEs) primarily move radially as they propagate away from the Sun, maintaining approximately constant angular width with respect to the Sun. As ICMEs have typical angular widths of around  $60^\circ$ , plasma elements on opposite flanks of an ICME separate in the non-radial direction at a speed,  $v_G$ , roughly equal to the ICME radial speed. This rapid expansion is a limiting factor on the propagation of information across an ICME at the local Alfvén speed,  $v_A$ . In this study, the 1-AU properties of ICMEs are used to compute two measures of ICME coherence. The first is the angular separation for which  $v_G$  exceeds the local  $v_A$ . The second measure is the angular extent over which a wavefront can propagate as an ICME travels from a given heliocentric distance to 1 AU. For both measures, ICMEs containing magnetic clouds show greater coherence than non-cloud ICMEs. However, even for magnetic clouds, information is unable to propagate across the full span of the structure. Thus interactions of ICMEs with other solar wind structures in the heliosphere are likely to lead to localised distortion, rather than solid-body like deflection. For magnetic clouds, the coherence length scale is significantly greater near the centre of the spacecraft encounter than at the leading or trailing edges. This suggests that magnetic clouds may be more coherent, and thus less prone to distortion, along the direction of the magnetic flux-rope axis than in directions perpendicular to the axis.

**Keywords** Coronal mass ejections · Solar wind

## 1. Introduction

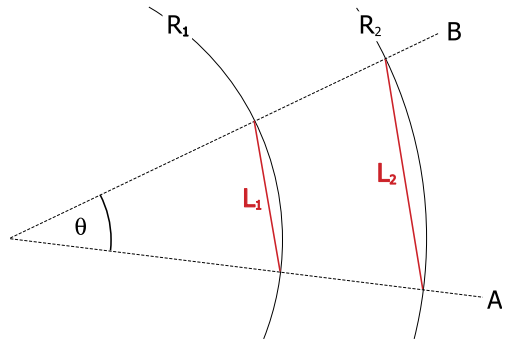
Coronal mass ejections (CMEs) are huge eruptions of solar plasma and magnetic flux (Webb and Howard, 2012). Their interplanetary manifestations, ICMEs, can drive severe space weather (Gosling, 1993), making them of both scientific and societal interest (Cannon et al., 2013).

---

✉ M.J. Owens  
[m.j.owens@reading.ac.uk](mailto:m.j.owens@reading.ac.uk)

<sup>1</sup> Department of Meteorology, University of Reading, Earley Gate, PO Box 243, Reading RG6 6BB, UK

**Figure 1** Radial directions A and B are separated by a constant angle  $\theta$ . At a radial distance  $R_1$ , they are separated by a distance  $L_1$ . At radial distance  $R_2$ , they are separated by  $L_2$ .



When observed close to the Sun, CMEs typically span around  $60^\circ$  with respect to the Sun, though much larger angular extents are also seen (Gopalswamy et al., 2008; Yashiro et al., 2004). In the outer corona and heliosphere, CMEs are observed to maintain approximately constant angular width as they propagate anti-sunward (Zhao et al., 2017; Helcats et al., 2018). Figure 1 shows two solar wind elements within an ICME, moving radially and separated by a constant angle  $\theta$  with respect to the Sun. In a time  $\Delta t$ , the plasma moves from  $R_1$  to  $R_2$ . Thus due to the spherical expansion of the solar wind, the two elements change their separation from  $L_1$  to  $L_2$ , giving

$$\sin(\theta/2) = \frac{L_1}{2R_1} = \frac{L_2}{2R_2}. \quad (1)$$

Therefore

$$\frac{\Delta R}{\Delta t} \sin(\theta/2) = \frac{1}{2} \frac{\Delta L}{\Delta t}. \quad (2)$$

If the radial speed,  $v_R$ , is constant,  $\Delta R/\Delta t = dR/dt = v_R$ . The two elements are therefore moving apart at the geometric expansion speed,  $v_G$ , given by

$$v_G = \frac{dL}{dt} = 2v_R \sin(\theta/2). \quad (3)$$

For a typical CME with  $\theta = 60^\circ$ ,  $\sin(\theta/2) = 0.5$  and thus  $v_G = v_R$ .

When observed *in situ* in near-Earth space, ICMEs are typically found to be radially expanding at a rate proportional to their bulk speed (Owens et al., 2005). This is in broad agreement with statistical studies of ICME duration (and hence radial width) at various heliocentric distances (Savani et al., 2011a). As the 1-AU radial expansion speed is relatively small (around 5–10% of  $\langle v_R \rangle$ ), it must also be small relative to  $v_G$  across the CME as a whole. Therefore the cross section of an ICME will rapidly flatten, or ‘pancake’ (Riley and Crooker, 2004; Savani et al., 2011b). (This is also illustrated in Figure 5.) This pancaking has been inferred from Heliographic Imager (HI, Eyles et al., 2009) observations of ICMEs (e.g., Savani et al., 2012).

The solar wind is a structured medium. During transit to 1 AU (and beyond), ICMEs undergo interaction with other solar wind structures, such as stream interaction regions (SIRs), as well as other ICMEs (e.g., Lugaz et al., 2012). Remote observations of ICME-ICME collisions in the heliosphere have been explained in terms of the interaction of solid-like bodies (Shen et al., 2012). Most ‘geometric’ models used for the interpretation of HI observations assume that ICMEs are coherent structures which are not significantly distorted by

the solar wind (e.g., Thernisien, Vourlidas, and Howard, 2009; Davies et al., 2012). Similarly, flux-rope models, used for the interpretation of the global structure of magnetic clouds on the basis of local observations, also assume simple, coherent structures (Burlaga et al., 1998; Démoulin and Dasso, 2009; Hidalgo et al., 2002; Owens, Merkin, and Riley, 2006). The rapid geometric expansion of ICMEs, however, may place limits on the coherence of ICMEs. Using average properties of ICMEs at 1 AU and a model for the associated variations with heliocentric distance, it has been argued that for most ICMEs  $v_G$  soon exceeds the local Alfvén speed,  $v_A$  (Owens, Lockwood, and Barnard, 2017). Thus information cannot propagate across ICMEs and they are unable to behave as coherent, solid-like structures even if the magnetic curvature forces would be sufficient in magnitude to resist the external deformation forces (Owens, Lockwood, and Barnard, 2017).

Conversely, current operational forecasting of ICMEs assumes that they are purely hydrodynamic structures (Odstrčil, Riley, and Zhao, 2004), and thus have very little coherence in the non-radial directions. This is highlighted by one-dimensional hydrodynamic simulations of ICMEs producing similar results to three-dimensional magnetohydrodynamic simulations (Owens et al., 2020).

Both of these approximations—complete coherence and complete incoherence of ICMEs—are valuable for making progress in their respective areas and will be more or less appropriate under different conditions. It is therefore valuable to assess and quantify the coherence of ICMEs.

This study builds on the work of Owens, Lockwood, and Barnard (2017). Two measures of ICME coherence are considered. In Sections 2 and 3, 1-AU properties are used to compute  $\theta_{\text{MAX}}$ , the angular separation for which  $v_G$  exceeds the local  $v_A$ . Specifically, in Section 2 the average 1-AU properties in ICMEs are considered for different ICME types, then Section 3 further subdivides the data by considering the properties at different times through an ICME as it passes 1 AU. The second measure of ICME coherence,  $\theta_C$ , is the angular extent that can be traversed by an Alfvén wavefront as the ICME propagates from a given point in the inner heliosphere to 1 AU. Thus in Section 4, the time history of the ICME interaction and its subsequent evolution are taken into account.

## 2. Mean Properties

Solar wind plasma and magnetic field properties in near-Earth space are obtained from the 1-hour OMNI data set from the Space Physics Data Facility (King and Papitashvili, 2005). Data in the period 1-1-1995 to 31-12-2019 are considered. ICME timings and classifications in near-Earth space are provided by Richardson and Cane (2010) and these authors' updated on-line ICME list. In the Richardson and Cane (2010) catalogue, ICMEs are classified into three Types. Type 2 are magnetic clouds (MCs), that is, ICMEs which show clear features of a magnetic cloud, having enhanced magnetic field intensity ( $> 10$  nT), smooth rotation in the magnetic field direction through a large angle, low proton temperatures and low plasma beta (Klein and Burlaga, 1982; Lepping, Jones, and Burlaga, 1990). Type 1 ICMEs, which are referred to as 'MC-like' ICMEs in the remainder of this study, show evidence of a magnetic field rotation, but lack some of the other features of MCs. Type 0 ICMEs are here referred to as 'non-MC' ICMEs as they lack most of the features of a typical magnetic cloud, such as an enhanced magnetic field intensity and magnetic field rotation.

For each of the 512 ICMEs in this period, the mean proton number density,  $n_p$ , radial solar wind speed,  $v_R$ , and magnetic field intensity,  $B$  are computed. Averages are taken over the whole ICME body (i.e., between the leading and trailing ICME boundaries) but

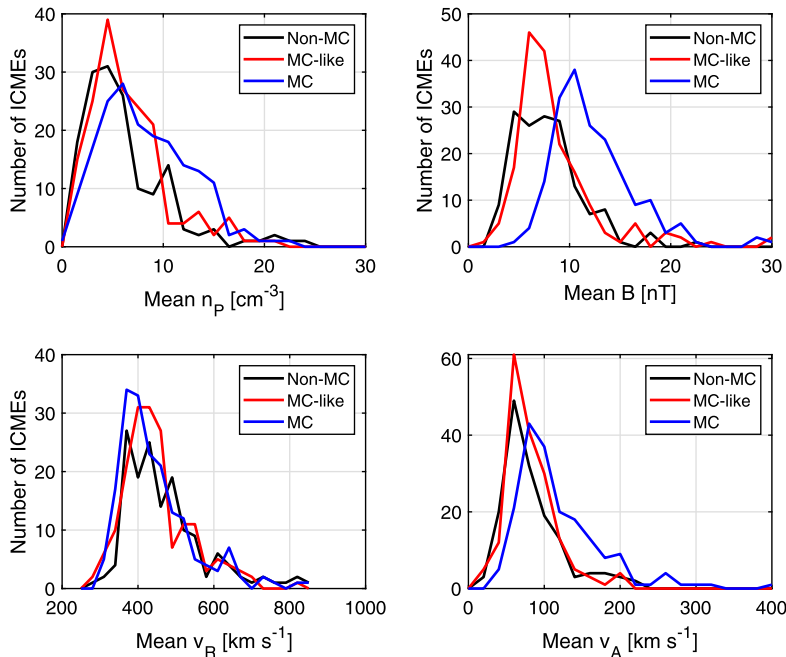


**Figure 2** Histograms of mean ICME properties at 1 AU. Properties are proton number density,  $n_p$  (top left), heliospheric magnetic field intensity,  $B$  (top right), radial solar wind speed,  $v_R$  (bottom left) and the Alfvén speed,  $v_A$ , computed from mean ICME properties (bottom right). Blue, red and black lines show histograms for magnetic cloud-like and non-cloud ICMEs, respectively.

do not include any sheath region ahead of the ICME. Figure 2 shows histograms of these average properties, with ICMEs further divided in magnetic clouds (MCs), magnetic cloud-like (MC-like) and non-magnetic cloud (non-MC) ICMEs. It can be seen that at 1 AU, typical mean  $n_p$  within ICMEs is around  $5 \text{ cm}^{-3}$ , with MCs showing a longer tail to the distribution out past  $10 \text{ cm}^{-3}$ . Mean  $v_R$  is similar in all ICME types, with modal values around  $400 \text{ km s}^{-1}$ . The main difference between MC and non-MC ICMEs is seen in the mean  $B$ , where non-MC- and MC-like CMEs have typical values around 6 nT, but MCs are around 11 nT. Of course, the classification of an ICME as an MC requires enhanced  $B$ , so this is unsurprising.

Using these bulk properties, we compute the Alfvén speed,  $v_A$ , as

$$v_A = \frac{B}{\sqrt{\mu_0 n_p m_p}}, \quad (4)$$

where  $\mu_0$  is the magnetic permeability of free space and  $m_p$  is the proton mass. Thus we are assuming for simplicity that the solar wind is a proton plasma. In reality, the contribution from helium ions means that  $v_A$  would be up to 10% lower than our estimate and ICME coherence would decrease. Given the more limited availability of helium data relative to proton, this is deemed acceptable for the current study. Figure 2 shows that in non-MC- and MC-like ICMEs,  $v_A$  based on mean ICME properties at 1 AU is typically around  $60 \text{ km s}^{-1}$ , whereas it is elevated in MCs, around  $90 \text{ km s}^{-1}$ , with a much longer tail to the distribution above  $120 \text{ km s}^{-1}$ .

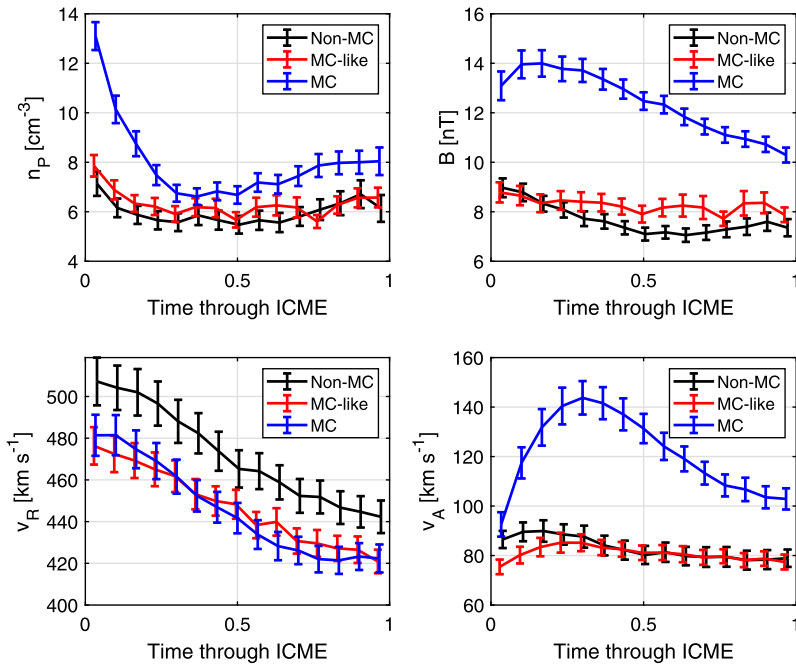


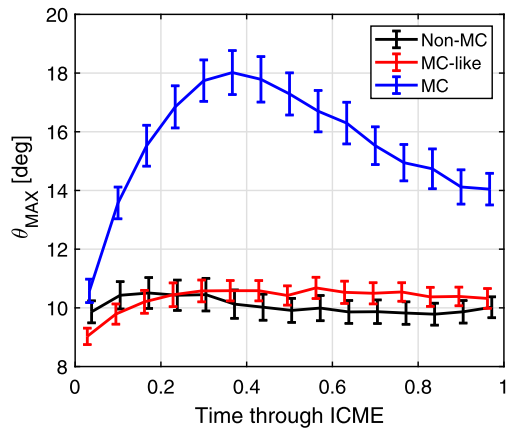
**Figure 3** Superposed epoch analysis of ICME properties at 1 AU between the ICME leading and trailing edges. ICMEs have been scaled to have a duration of unity. Blue, red and black lines show magnetic cloud-like and non-cloud ICMEs, respectively. Error bars show one standard error on the mean.

The maximum coherence angle,  $\theta_{\text{MAX}}$ , is the angular separation of solar wind elements for which  $v_G = v_a$ , i.e., where information travels at the same speed as the geometric expansion and thus is unable to effectively propagate. Taking the average properties of non-MC- and MC-like ICMEs, this gives  $\theta_{\text{MAX}} = 17^\circ$ . For MCs, this is slightly higher at  $26^\circ$ . Despite being upper limits, both these values are well below the typical angular width of CMEs of around  $60^\circ$  (Yashiro et al., 2004). However, average properties could be misleading if there are systematic variations in Alfvén speed within ICMEs, as investigated in the next section.

### 3. ICME Profiles

In this section we consider ICME time series, assumed to approximate a radial profile though an ICME. In order to account for the different durations of ICME encounters at 1 AU, each ICME time series is scaled to have a duration of unity. The resulting superposed epoch analysis is shown in Figure 3. Error bars are one standard error on the mean. Firstly, taking the  $v_R$  profiles, all ICMEs show a similar drop in  $v_R$  from the leading to trailing edge, indicative of a similar degree of radial expansion as they pass over the observing spacecraft. This is expected given their comparable average radial speeds (Owens et al., 2005), though MC-like ICMEs do display a slightly higher average speed. The  $n_p$  profiles display evidence of expansion; lowest values near the ICME centre, and compression near the leading edge, owing to the ICME expansion into the solar wind upstream. This is most apparent for MCs. The  $B$  profiles for non-MC- and MC-like ICMEs show little variation, except for possible weak

**Figure 4** The angular separation,  $\theta_{\text{MAX}}$ , for which the geometry expansion speed,  $v_G$ , is equal to the local Alfvén speed, as a function of time through ICME. Error bars are one standard error on the mean.



compression near the leading edge. For MC profiles, it is worth first considering the expectation: A spacecraft encounter with a force-free flux rope (Burlaga, 1988) would produce a ‘domed’ profile with a maximum at the closest approach to the flux-rope axis, near the centre of the encounter. Radial expansion of the flux rope as it passes over the observer would instead lead to a slightly asymmetric time series, as more time is spent in the trailing than leading portion of the flux rope. Here, the MC  $B$  series is highly asymmetric, suggesting the expansion is also leading to compression of the leading edge and rarefaction of the trailing edge. This could also be caused by the duration of the identified ICME being longer than the duration of the embedded flux-rope structure.

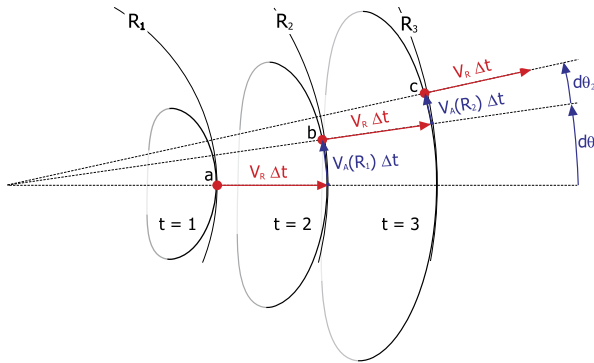
The ICME properties combine to give reasonably flat  $v_A$  profiles for non-MC- and MC-like ICME, except for a small enhancement near the leading edge. Note that the non-linear combination of parameters means that the average  $v_A$  computed in this way is significantly higher than using the ICME-averaged  $n_p$  and  $B$  parameters in Section 2, being around  $80 \text{ km s}^{-1}$  versus  $60 \text{ km s}^{-1}$ . For MCs, the average  $v_A$  is also significantly elevated compared to the estimates based on mean  $n_p$  and  $B$ . There is also a systematic variation in  $v_A$  with time, from around  $90 \text{ km s}^{-1}$  at the MC leading edge, peaking around  $140 \text{ km s}^{-1}$  around a third of the way through the MC, and dropping back to just over  $100 \text{ km s}^{-1}$  at the trailing edge.

Figure 4 shows  $\theta_{\text{MAX}}$ , the angular separation for which the geometric expansion speed is equal to the local Alfvén speed, computed using  $v_A$  at different times through the ICME and for different ICME types. For non-cloud and cloud-like ICMEs, the small variation in  $v_A$  through the ICME is effectively counteracted by the  $v_R$  variation to produce almost constant  $\theta_{\text{MAX}}$  at around  $10^\circ$ . For magnetic cloud ICMEs, the enhanced  $v_R$  and reduced  $v_A$  at the leading edge act together to reduce  $\theta_{\text{MAX}}$  with respect to both the centre of magnetic clouds and the trailing edge. Thus  $\theta_{\text{MAX}}$  varies from around  $10^\circ$  at the leading edge, to a maximum value of around  $18^\circ$  around a third of the way through the magnetic cloud, to approximately  $14^\circ$  at the trailing edge.

#### 4. Effect of Previous Time History

This section investigates the effect of time history on ICME coherence. Consider an ICME at some heliocentric distance  $R_i$  that undergoes a localised perturbation, such as by the





**Figure 5** A schematic of the model set-up used to estimate the time history of ICME coherence. At time  $t = 1$ , the ICME leading edge is at radius  $R_1$ . Each point on the ICME leading edge moves radially at speed  $v_R$ . Information propagates out from point (a) at the leading edge of the ICME at speed  $v_A(R_1)$ . By time  $t = 2$ , it reaches point (b), at an angular separation of  $d\theta_1$ . Now information propagates from (b) at speed  $v_A(R_2)$ . Thus by time  $t = 3$ , it has reached point (c), which is an additional angular separation of  $d\theta_2$ . This iterative process is performed from the radial distance at which the ICME is first perturbed (e.g., by interaction with a solar wind structure) to 1 AU.

interaction with a solar wind stream. A wavefront will propagate out through the ICME from the point of perturbation. The maximum distance over which the ICME can be considered coherent at 1 AU can be quantified by  $\theta_C$ , the maximum angular separation (with respect to the Sun) that a wavefront can traverse during the time the ICME travels from  $R_i$  1 AU.

There are three reasons why  $\theta_C$  will be a strong function of  $R_i$ . Firstly, and most obviously, the earlier the perturbation occurs, the more time there is for information to propagate across the ICME. Secondly, a given linear distance subtends a greater angular distance closer to the Sun. Thirdly, the Alfvén speed within the ICME is expected to be much higher closer to the Sun (owing to conservation of magnetic flux and ICME expansion), so information can travel more rapidly when the ICME is close to the Sun.

In order to quantify the net result of these effects, a simple numerical model is used, as shown in Figure 5. Using a small time step, the ICME is advanced in heliocentric distance at a constant speed  $v_R$ . A time step of 17 s is used, as  $v_R = 400 \text{ km s}^{-1}$  results in a radial increment of 0.01 solar radii. Smaller time steps give the same result to within numerical round off, suggesting convergence has been reached. Starting from the point of perturbation, at each time step a wavefront propagates at the local Alfvén speed,  $v_A(R)$ . As  $B$  and  $n_p$  scale differently with  $R$ , the resulting  $v_A(R)$  will be a function of the heliocentric distance. As discussed further below,  $B(R)$  and  $n_p(R)$  are estimated from the (known) 1-AU values. By summing the individual angular changes at each time step, it is possible to estimate  $\theta_C$  for a range of  $R_i$  and 1-AU ICME properties.

Estimates of  $B(R)$  and  $n_p(R)$  within ICMEs are required to determine the radial variation of  $v_A$ . While there have been attempts to estimate such radial trends purely on the basis of in-situ observations, in practice such studies utilise observations of many different ICMEs at various radial distances (Savani et al., 2011b; Bothmer and Schwenn, 1998), rather than the evolution of a single ICME at many distances. Given the relatively limited number of events available for study within 1 AU and the large degree of event-to-event variability between ICMEs, the radial trends are poorly constrained in this manner. Multiple observations of the same ICME at different radial distances are rare and the observing spacecraft are typically only approximately radially aligned. Furthermore, the observations are typically fortuitous

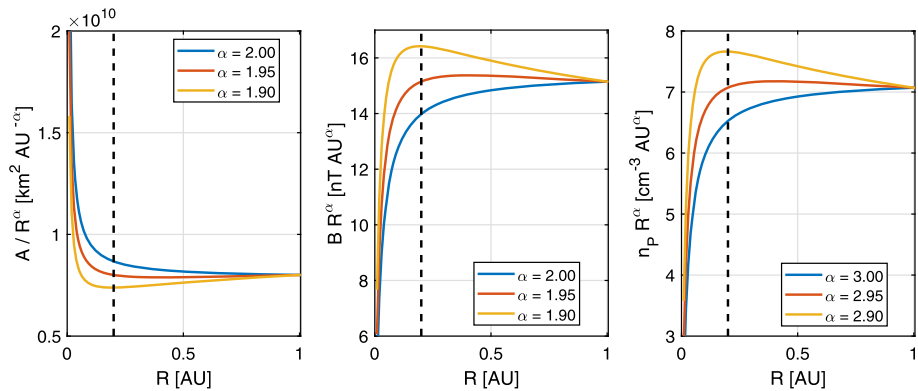


**Figure 6** Left: Variation with radial distance,  $R$ , of cross-sectional area,  $A$ , of a kinematically-distorted ICME, assuming a 1-AU value of  $6 \times 10^9 \text{ km}^2$ . Middle: Magnetic field intensity,  $B$ , within the ICME, assuming a 1-AU value of 15 nT. Right: Proton density,  $n_p$ , within the CME, assuming a 1-AU value of  $7 \text{ cm}^{-3}$ . Past 0.2 AU (indicated by the vertical dashed lines),  $A$  scales approximately as  $R^{1.95}$ ,  $B$  as  $R^{-1.95}$ , and  $n_p$  as  $R^{-2.95}$ .

alignments with planetary missions which cannot always make suitable measurements of the solar wind plasma (e.g., Good et al., 2015; Salman, Winslow, and Lugaz, 2020), making estimates of  $n_p(R)$  particularly problematic. Finally, until the recent launch of Parker Solar Probe, no in-situ ICME observations were available at all inside 0.3 AU.

Instead,  $B(R)$  and  $n_p(R)$  are here estimated using physics-based scaling relations applied to the abundant ICME observations at 1 AU. The obtained relations lie within the observational spread of the radial trends (e.g., Savani et al., 2011a). A kinematically-distorted flux-rope model (Owens, Merkin, and Riley, 2006) is used for this purpose. In this model, the ICME is assumed to begin life close to the Sun with a circular cross section, which then distorts due to two motions: radial propagation in spherical geometry, as with the ambient solar wind, and expansion in the radial direction due to high internal pressure relative to the ambient solar wind. This is shown by ICME outlines of Figure 5. Radial motion results in the cross-sectional flattening, or ‘pancaking’, of ICMEs both predicted theoretically (Riley and Crooker, 2004) and inferred from Heliospheric Imager observations of CMEs (e.g., Savani et al., 2012).

The left-hand panel of Figure 6 shows how  $A$ , the cross-sectional area of a kinematically-distorted ICME, varies with radial distance from the Sun,  $R$ . Note that as  $A$  increases with  $R$ , for plotting purposes  $A$  has been scaled by a factor  $1/R^\alpha$ , where results for three values of  $\alpha$  around 2 are shown. Close to the Sun ( $R < 0.2$  AU),  $A$  increases more rapidly than  $R^2$ . This corresponds to the rapid distortion of the ICME cross section from circular to a ‘pancake’ structure. After 0.2 AU, however,  $A$  varies as approximately  $R^{1.95}$ .

If the magnetic flux contained within the ICME is conserved, then  $B$  is inversely proportional to  $A$ . This is shown in the middle panel of Figure 6, where  $B(R)$  varies as  $R^{-1.95}$  past 0.2 AU. Erosion of the magnetic flux from the ICME by reconnection would break magnetic flux conservation within an ICME, but this is expected to be a very small factor (Ruffenach et al., 2015). The radial variation in the plasma density within the ICME can be estimated if the mass inside an ICME is assumed to be conserved. In this case, the density scales inversely with the volumetric increase of the ICME,  $RA(R)$ . As  $A(R)$  scales as  $R^{1.95}$ , this means  $n_p(R)$  varies as  $R^{-2.95}$  beyond 0.2 AU. This is shown in the right-hand panel of

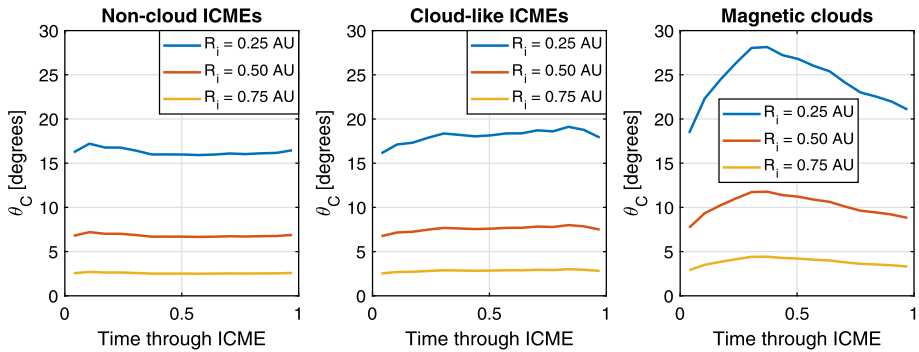


**Figure 7** Variation of the angular distance (with respect to the Sun) that information can propagate within ICMEs,  $\theta_C$ , for time through ICME, different ICME types (panels left to right) and different initial perturbation distances,  $R_i$ .

Figure 6. These scaling relations can be used to estimate  $B(R)$  and  $n_p(R)$  for an ICME on the basis of 1-AU values, and hence  $v_A$  between 0.2 and 1 AU. They are consistent with the radial trends inferred from the available observations (e.g., Salman, Winslow, and Lugaz, 2020, estimated that the maximum value of  $B$  within ICMEs scaled as  $R^{-1.91}$ , but there was considerable spread in the data. They did not consider plasma density with ICMEs).

Figure 7 shows  $\theta_C$ , the maximum angular distance a wavefront can travel by the time the ICME reaches 1 AU, for initial perturbation distances of  $R_i = 0.25, 0.5$  and  $0.75$  AU. For all ICME types and positions within an ICME,  $R_i$  has a large and non-linear effect on  $\theta_C$ . For non-cloud and cloud-like ICMEs, there is little variation in  $\theta_C$  through the duration of the ICME itself. For perturbations which occur beyond 0.5 AU,  $\theta_C$  is well below  $10^\circ$ . This should be contrasted with a typical CME angular extent of around  $60^\circ$ . Even for  $R_i = 0.25$  AU,  $\theta_C$  remains below  $20^\circ$ , less than a third of the typical ICME angular extent.

For magnetic clouds, the picture is more complex. Near the MC leading edge,  $\theta_C$  is similar to cloud-like ICMEs. Around one third of the way through the ICME, where the Alfvén speed peaks at 1 AU,  $\theta_C$  also peaks. For  $R_i = 0.25$  AU,  $\theta_C$  reaches a maximum value of  $27^\circ$ , whereas it peaks at  $12^\circ$  and  $4.5^\circ$  for  $R_i = 0.5$  and  $0.75$  AU, respectively. Thus, even for optimum conditions,  $\theta_C$  it remains below half the typical CME angular extent.

## 5. Discussion

Interplanetary coronal mass ejections (ICMEs) are huge, expanding structures. Consequently, the finite travel time of information across an ICME can inhibit its ability to behave as a single, coherent structure. This study has investigated two measures of the coherence of ICMEs at 1 AU.

The first part of the study used average 1-AU properties of ICMEs to determine  $\theta_{MAX}$ , the angular span over which the geometric speed of separation of plasma parcels owing to spherical expansion,  $v_G$ , is equal to the local Alfvén speed,  $v_A$ . Once this condition is met, information can no longer propagate over such distances and the ICME cannot be considered a coherent structure over such scales. ICMEs were separated into three categories. Magnetic clouds (MCs) are ICMEs which display an enhanced magnetic field intensity and smooth rotation in the magnetic field direction, as well as reduced plasma temperature and density. Cloud-like ICMEs are here defined as ICMEs with some magnetic field rotation,

but that do not meet the full MC definition. And non-cloud ICMEs lack most or all of the features of an MC. For non-cloud and cloud-like ICMEs, there is no significant variation in  $\theta_{\text{MAX}}$  as the ICME passes 1 AU. Although these ICMEs are expanding and thus exhibit a systematic variation in  $v_R$  and hence  $v_G$ , they also show a small variation in magnetic field intensity and proton density which produces a commensurate variation in  $v_A$ . Thus  $\theta_{\text{MAX}}$  remains approximately  $10^\circ$  throughout non-cloud and cloud-like ICMEs. For ICMEs containing magnetic clouds, this is not the case. The magnetic field intensity peaks very close to the ICME leading edge, but the proton density is also enhanced there, leading to a relatively low  $v_A$ . Approximately one third of the way through the ICME,  $v_A$  peaks. Coupled with the declining  $v_G$  variation,  $\theta_{\text{MAX}}$  peaks at around 0.4 of the ICME duration, at a value of around  $18^\circ$ .  $\theta_{\text{MAX}}$  in the trailing portion of a magnetic cloud is also around 50% higher than in the leading portion.

Interpreting  $\theta_{\text{MAX}}$  is difficult for two reasons. Firstly, it is based on the local magnetic field and plasma properties, which are only representative of the conditions at 1 AU. Secondly,  $\theta_{\text{MAX}}$  is the limiting case where information can no longer propagate. But in practice, an ICME will cease to be coherent long before this criterion is met; when the wavefront travel time is longer than the ICME travel time between two points, the ICME will effectively cease to be coherent.

The second part of the study attempted to address these two limitations and provide a more meaningful measure of ICME coherence by considering the time history prior to the ICME arriving at 1 AU. Using a model for the ICME expansion it is assumed that the magnetic field intensity and proton density can be reconstructed between 0.2 and 1 AU by simple radial scaling of the measured 1-AU values. To achieve this, the magnetic flux and mass content of an ICME is assumed to be constant and a simple physics-based model of ICME cross-sectional evolution was used. In this way, the local value of  $v_A$  can be estimated as an ICME propagates from 0.2 to 1 AU. Three scenarios were considered, wherein the ICME undergoes local perturbation at distances of  $R_i = 0.25, 0.5$  and  $0.75$  AU. By integrating the maximum angular motion of a wavefront during ICME transit from  $R_i$  to 1 AU, the maximum coherence angle at 1 AU,  $\theta_C$ , was computed. This was performed for different ICME types and using 1-AU properties at different times through the ICME. For non-cloud and cloud-like ICMEs, there is no significant variation through the duration of the ICME and the controlling factor in  $\theta_C$  is how early in the CME's life the perturbation occurs. However, even a perturbation at 0.25 AU can travel across less than one third of the ICME extent by the time the ICME reaches 1 AU. For perturbations at 0.5 and 0.75 AU, information can propagate across only 10% and 5%, respectively, of a typical ICME extent. For magnetic clouds, the leading edge behaves similar to non-cloud and cloud-like ICMEs. Near the centre of the magnetic clouds, however,  $\theta_C$  is significantly elevated, reaching approximately  $27^\circ$  for  $R_i = 0.25$  AU, which is approximately half the typical angular span of an ICME.

Thus both measures of ICME coherence suggest that:

- i) ICME perturbations in the heliosphere beyond 0.25 AU are unable to propagate over the whole ICME extent.
- ii) The scale over which ICMEs can be considered coherent (i.e., the scale over which information can propagate) varies significantly with ICME type.
- iii) For cloud-like and non-cloud ICMEs, there is little variation in coherence length within the structure in the radial direction.
- vi) The enhanced magnetic field strength, and hence Alfvén speed, within magnetic clouds means they are coherent over larger spatial scales than non-cloud and cloud-like ICMEs.

- v) For magnetic clouds, there is significant variation within the ICME in coherence length, with the lowest values at the leading edge and the peak value approximately 0.4 of the way through the structure.

Thus, for ICMEs in the heliosphere (here taken to be beyond 0.2 AU), information is unable to propagate across their full span. This is true even for magnetic clouds, which exhibit enhanced magnetic field intensity, and hence wave speed and coherence, compared with other ICMEs. As proposed in Owens, Lockwood, and Barnard (2017), this means that the heliospheric interaction of an ICME with other solar wind structures will lead to local distortion, rather than a solid-body like deflection of the centre of mass of the ICME. Furthermore, the enhanced coherence length near the centre of magnetic clouds suggests that there is preferential information propagation along the axis of flux ropes. Thus magnetic clouds may display more coherence along the axial direction than perpendicular to the axis.

It is worth noting the limitations and implicit assumptions with the analysis presented in this study. Most prominently, the model of the CME cross-sectional evolution, which is used to estimate the Alfvén speed at a range of heliocentric distances, assumes a purely kinematic distortion. Thus any resistance to deformation from the internal magnetic field structure of ICMEs is ignored. Similarly, while the ability of information to propagate across an ICME has been investigated, this does not directly say anything about the ability of an ICME to ‘use’ this information in order to resist deformation by external factors. This is contingent on the relative magnetic curvature and dynamic pressure forces. Thus it is desirable to further investigate ICME coherence using three-dimensional magnetohydrodynamic simulations of magnetic flux ropes (e.g., Török et al., 2018).

**Acknowledgements** OMNI data are available from <https://omniweb.gsfc81.nasa.gov/>. The updated Cane and Richardson near-Earth CME list is available from <http://www.srl.caltech.edu/ACE/ASC/DATA/level3/icmetable2.htm>. MO is part-funded by Science and Technology Facilities Council (STFC) grant number ST/R000921/1, and Natural Environment Research Council (NERC) grant number NE/P016928/1.

**Disclosure of Potential Conflict of Interest** I declare I have no conflicts of interest.

**Publisher’s Note** Springer Nature remains neutral with regard to jurisdictional claims in published maps and institutional affiliations.

**Open Access** This article is licensed under a Creative Commons Attribution 4.0 International License, which permits use, sharing, adaptation, distribution and reproduction in any medium or format, as long as you give appropriate credit to the original author(s) and the source, provide a link to the Creative Commons licence, and indicate if changes were made. The images or other third party material in this article are included in the article’s Creative Commons licence, unless indicated otherwise in a credit line to the material. If material is not included in the article’s Creative Commons licence and your intended use is not permitted by statutory regulation or exceeds the permitted use, you will need to obtain permission directly from the copyright holder. To view a copy of this licence, visit <http://creativecommons.org/licenses/by/4.0/>.

## References

- Bothmer, V., Schwenn, R.: 1998, The structure and origin of magnetic clouds in the solar wind. *Ann. Geophys.* **16**, 1.
- Burlaga, L.F.: 1988, Magnetic clouds: Constant alpha force-free configurations. *J. Geophys. Res.* **93**, 7217. DOI.
- Burlaga, L., Fitzenreiter, R., Lepping, R., Ogilvie, K., Szabo, A., Lazarus, A., Steinberg, J., Gloeckler, G., Howard, R., Michels, D., Farrugia, C., Lin, R.P., Larson, D.E.: 1998, A magnetic cloud containing prominence material – January 1997. *J. Geophys. Res.* **10**, 277. DOI.

- Cannon, P., Angling, M., Barclay, L., Curry, C., Dyer, C., Edwards, R., Greene, G., Hapgood, M., Horne, R.B., Jackson, D.: 2013, *Extreme Space Weather: Impacts on Engineered Systems and Infrastructure*, Royal Academy of Engineering, London. 1-903496-95-0.
- Davies, J.A., Harrison, R.A., Perry, C.H., Möstl, C., Lugaz, N., Rollett, T., Davis, C.J., Crothers, S.R., Temmer, M., Eyles, C.J., Savani, N.P.: 2012, A self-similar expansion model for use in solar wind transient propagation studies. *Astrophys. J.* **750**, 23. DOI.
- Démoulin, P., Dasso, S.: 2009, Magnetic cloud models with bent and oblate cross-section boundaries. *Astron. Astrophys.* **507**, 969. DOI.
- Eyles, C.J., Harrison, R.A., Davis, C.J., Waltham, N.R., Shaughnessy, B.M., Mapson-Menard, H.C.A., Bewsher, D., Crothers, S.R., Davies, J.A., Simnett, G.M.: 2009, The heliospheric imagers onboard the STEREO mission. *Solar Phys.* **254**, 387. DOI.
- Good, S.W., Forsyth, R.J., Raines, J.M., Gershman, D.J., Slavin, J.A., Zurbuchen, T.H.: 2015, Radial evolution of a magnetic cloud: Messenger, STEREO and Venus Express observations. *Astrophys. J.* **807**, 177. DOI.
- Gopalswamy, N., Yashiro, S., Michalek, G., Stenborg, G., Vourlidas, A., Freeland, S., Howard, R.: 2008, The SOHO/LASCO CME catalog. *Earth Moon Planets* **104**, 295. DOI.
- Gosling, J.T.: 1993, The solar flare myth. *J. Geophys. Res.* **98**, 18937. DOI.
- Helcats, E., Barnes, D., Davies, J.A., Harrison, R.: 2018, HELCATS HCME\_wp2\_v03. DOI. [https://figshare.com/articles/dataset/HELCATS\\_HCME\\_WP2\\_V03/5803152](https://figshare.com/articles/dataset/HELCATS_HCME_WP2_V03/5803152).
- Hidalgo, M.A., Cid, C., Vinas, A.F., Sequeiros, J.: 2002, A non-force-free approach to the topology of magnetic clouds. *J. Geophys. Res.* **107**, 2156. DOI.
- King, J.H., Papitashvili, N.E.: 2005, Solar wind spatial scales in and comparisons of hourly wind and ACE plasma and magnetic field data. *J. Geophys. Res.* **110**, A02104. DOI.
- Klein, L.W., Burlaga, L.F.: 1982, Interplanetary magnetic clouds at 1 AU. *J. Geophys. Res.* **87**, 613.
- Lepping, R.P., Jones, J.A., Burlaga, L.F.: 1990, Magnetic field structure of interplanetary clouds at 1 AU. *J. Geophys. Res.* **95**, 11957. DOI.
- Lugaz, N., Farrugia, C.J., Davies, J.A., Möstl, C., Davis, C.J., Roussev, I.I., Temmer, M.: 2012, The deflection of the two interacting coronal mass ejections of 2010 May 23–24 as revealed by combined in situ measurements and heliospheric imaging. *Astrophys. J.* **759**, 68. DOI.
- Odstrcil, D., Riley, P., Zhao, X.-P.: 2004, Numerical simulation of the 12 May 1997 interplanetary CME event. *J. Geophys. Res.* **109**, A02116. DOI.
- Owens, M.J., Lockwood, M., Barnard, L.A.: 2017, Coronal mass ejections are not coherent magnetohydrodynamic structures. *Sci. Rep.* **7**, 4152. DOI.
- Owens, M.J., Merkin, V.G., Riley, P.: 2006, A kinematically distorted flux rope model for magnetic clouds. *J. Geophys. Res.* **111**, A03104. DOI.
- Owens, M.J., Cargill, P.J., Pagel, C., Siscoe, G.L., Crooker, N.U.: 2005, Characteristic magnetic field and speed properties of interplanetary coronal mass ejections and their sheath regions. *J. Geophys. Res.* **110**, 1. DOI.
- Owens, M.J., Lang, M., Barnard, L., Riley, P., Ben-Nun, M., Scott, C.J., Lockwood, M., Reiss, M.A., Arge, C.N., Gonzi, S.: 2020, A computationally efficient, time-dependent model of the solar wind for use as a surrogate to three-dimensional numerical magnetohydrodynamic simulations. *Solar Phys.* **295**, 43. DOI.
- Richardson, I.G., Cane, H.V.: 2010, Near-Earth interplanetary coronal mass ejections during Solar Cycle 23 (1996–2009): Catalog and summary of properties. *Solar Phys.* **264**, 189. DOI.
- Riley, P., Crooker, N.U.: 2004, Kinematic treatment of CME evolution in the solar wind. *Astrophys. J.* **600**, 1035. DOI.
- Ruffenach, A., Lavraud, B., Farrugia, C.J., Démoulin, P., Dasso, S., Owens, M.J., Sauvaud, J., Rouillard, A.P., Lynnyk, A., Foulon, C.: 2015, Statistical study of magnetic cloud erosion by magnetic reconnection. *J. Geophys. Res.* **120**, 43. DOI.
- Salman, T.M., Winslow, R.M., Lugaz, N.: 2020, Radial evolution of coronal mass ejections between MESSENGER, Venus Express, STEREO, and L1: Catalog and analysis. *J. Geophys. Res.* **125**, e2019JA027084. DOI.
- Savani, N.P., Owens, M.J., Rouillard, A.P., Forsyth, R.J., Kusano, K., Shiota, D., Kataoka, R.: 2011a, Evolution of coronal mass ejection morphology with increasing heliocentric distance. I. Geometrical analysis. *Astrophys. J.* **731**, 109. DOI.
- Savani, N.P., Owens, M.J., Rouillard, A.P., Forsyth, R.J., Kusano, K., Shiota, D., Kataoka, R., Jian, L., Bothmer, V.: 2011b, Evolution of coronal mass ejection morphology with increasing heliocentric distance. II. In situ observations. *Astrophys. J.* **732**, 117. DOI.
- Savani, N.P., Davies, J.A., Davis, C.J., Shiota, D., Rouillard, A.P., Owens, M.J., Kusano, K., Bothmer, V., Bamford, S.P., Lintott, C.J., Smith, A.: 2012, Observational tracking of the 2D structure of coronal mass ejections between the Sun and 1 AU. *Solar Phys.* **279**, 517. DOI.

- Shen, C., Wang, Y., Wang, S., Liu, Y., Liu, R., Vourlidas, A., Miao, B., Ye, P., Liu, J., Zhou, Z.: 2012, Super-elastic collision of large-scale magnetized plasmoids in the heliosphere. *Nat. Phys.* **8**, 923. [DOI](#).
- Thernisien, A., Vourlidas, A., Howard, R.A.: 2009, Forward modeling of coronal mass ejections using STEREO/SECCHI data. *Solar Phys.* **256**, 111. [DOI](#).
- Török, T., Downs, C., Linker, J.A., Lionello, R., Titov, V.S., Mikić, Z., Riley, P., Caplan, R.M., Wijaya, J.: 2018, Sun-to-Earth MHD simulation of the 2000 July 14 “Bastille Day” eruption. *Astrophys. J.* **856**, 75. [DOI](#).
- Webb, D.F., Howard, T.A.: 2012, Coronal mass ejections: Observations. *Living Rev. Solar Phys.* **9**, 3. [DOI](#).
- Yashiro, S., Gopalswamy, N., Michalek, G., St Cyr, O.C., Plunkett, S.P., Rich, N.B., Howard, R.A.: 2004, A catalog of white light coronal mass ejections observed by the SOHO spacecraft. *J. Geophys. Res.* **109**, A07105. [DOI](#).
- Zhao, X.H., Feng, X.S., Feng, H.Q., Li, Z.: 2017, Correlation between angular widths of CMEs and characteristics of their source regions. *Astrophys. J.* **849**, 79. [DOI](#).